



HAL
open science

Near-infrared observations of the gas structure and kinematics in the circumnuclear region of NGC 1672

Nastaran Fazeli, Andreas Eckart, Gerold Busch, Madeleine Yttergren, Françoise Combes, Persis Misquitta, Christian Straubmeier

► **To cite this version:**

Nastaran Fazeli, Andreas Eckart, Gerold Busch, Madeleine Yttergren, Françoise Combes, et al.. Near-infrared observations of the gas structure and kinematics in the circumnuclear region of NGC 1672. *Astronomy and Astrophysics - A&A*, 2020, 638, 10.1051/0004-6361/201937092 . insu-03718049

HAL Id: insu-03718049

<https://insu.hal.science/insu-03718049>

Submitted on 8 Jul 2022

HAL is a multi-disciplinary open access archive for the deposit and dissemination of scientific research documents, whether they are published or not. The documents may come from teaching and research institutions in France or abroad, or from public or private research centers.

L'archive ouverte pluridisciplinaire **HAL**, est destinée au dépôt et à la diffusion de documents scientifiques de niveau recherche, publiés ou non, émanant des établissements d'enseignement et de recherche français ou étrangers, des laboratoires publics ou privés.

Near-infrared observations of the gas structure and kinematics in the circumnuclear region of NGC 1672[★]

Nastaran Fazeli¹, Andreas Eckart^{1,2}, Gerold Busch¹, Madeleine Yttergren^{1,2}, Françoise Combes³, Persis Misquitta¹, and Christian Straubmeier¹

¹ I. Physikalisches Institut der Universität zu Köln, Zùlpicher Str. 77, 50937 Köln, Germany
e-mail: fazeli@ph1.uni-koeln.de

² Max-Planck-Institut für Radioastronomie, Auf dem Hügel 69, 53121 Bonn, Germany

³ LERMA, Observatoire de Paris, Collège de France, PSL Univ., CNRS, Sorbonne Univ., UPMC, 75014 Paris, France

Received 10 November 2019 / Accepted 2 April 2020

ABSTRACT

We present our near-infrared, integral-field spectroscopy observations of the central $550 \times 550 \text{ pc}^2$ ($10'' \times 10''$) of the local galaxy NGC 1672. Our aim is to investigate the morphology and kinematics of gas and stars to probe evidence for feeding and feedback phenomena. For this purpose the near-infrared wavelength regime and integral-field unit technique provide a vast amount of useful information. The narrow emission line ratios suggest that the galaxy hosts a low-luminosity active galactic nucleus. From the $M_{\text{BH}}-\sigma_*$ relation, we find a black hole mass of a few $10^7 M_\odot$. The total reservoir of hot molecular and ionised gas is estimated, using flux of H_2 and $\text{Br}\gamma$ emission lines, to be $258 M_\odot$ and $2.3 \times 10^6 M_\odot$ respectively. The most striking feature in the emission line flux maps is the star-forming ring at a radius of $\sim 3''$. The stellar and gaseous kinematics both show a rotation pattern in a disc that is blue-shifted in the north-west and red-shifted in the south-east. However, unlike the stellar kinematics, gas kinematics show various complexities, such as higher amplitudes in the central region (within the star-forming ring). The molecular gas velocity-field map shows deviations from pure disc motion in the form of an S-shaped zero-velocity line. In particular the position angle of the zero-velocity line changes in the central arcsecond, resembling the decoupled nuclear disc or molecular torus found in CO(3–2). There is an offset of $0'.5$ between the nuclear continuum barycentre and kinematic centre of molecular gas towards the north-west. The velocity field of $\text{Br}\gamma$ emitting gas on the other hand, is highly red-shifted in the centre and offset from the continuum emission peak by about $1''$. Investigating the spectra of this region we detect a doubled-horn $\text{Br}\gamma$ emission line in the nucleus and north-west. This region is also luminous in radio 3 cm emission connecting the nucleus to the star-forming ring.

Key words. infrared: galaxies – galaxies: nuclei – galaxies: kinematics and dynamics – galaxies: active – galaxies: Seyfert – galaxies: individual: NGC 1672

1. Introduction

Active galactic nuclei (AGN) are not only amongst the most energetic phenomena in the Universe but it is also suggested that these sources play a key role in the evolution of their host galaxy. This co-evolution is observed through, for example the well-established $M_{\text{BH}}-\sigma$ relation (Gültekin et al. 2009). In addition, AGN feedback is one of the key requirements in cosmological simulations to manufacture the galaxy population observed today (e.g. Springel et al. 2005). This phenomenon is mostly associated with jets or fast outflows of ionised and atomic gas (e.g. Veilleux et al. 2005; Fiore et al. 2017) that can extend up to several kiloparsecs from the centre.

On the other hand, the feeding processes that fuel the AGN and star formation are revealed in the kinematics and morphology of the molecular gas in circumnuclear regions. In the case of nearby galaxies with low-luminosity AGN the gravitational torques by non-axisymmetric potentials funnel the gas to the inner kiloparsec (e.g. García-Burillo et al. 2005; García-Burillo & Combes 2012; Combes et al. 2013, 2014). Several hydrodynamic and observational studies show that in many galaxies the gas brought by the bar gets stalled in a

nuclear ring at or near the inner Lindblad resonance (ILR). What happens to the gas from this point on is the subject of many recent studies. Subsequent dynamical instabilities such as bars-within-bars, warps or nuclear spirals, dynamical frictions, and viscosity are amongst the mechanisms suggested for funnelling the gas to within tens of parsecs of the SMBH (e.g. for hydrodynamic simulations and observational evidence; Martini et al. 2001; Hopkins & Quataert 2010; Smajić et al. 2014, 2015; Kim & Elmegreen 2017).

Integral-field unit (IFU) instruments alongside large radio interferometers have revolutionised the simultaneous study of the distribution and kinematics of both ionised and molecular gas at the same spatial scales. The near-infrared (NIR) wavelength region is particularly valuable, since it traces hot molecular and ionised gas and their excitation mechanisms, and reveals properties of the AGN, especially those properties with less extinction compared to the optical wavelength (Smajić et al. 2012). Therefore integral-field spectroscopy (IFS) in the NIR is ideal to study stellar populations and star formation in (dust-obscured) centres of galaxies.

This paper continues our previous work on a sample of nearby galaxies (NGC 1433, NGC 1566: Smajić et al. 2014, 2015, NGC 1808: Busch et al. 2017, NGC 1365: Fazeli et al. 2019, and NGC 1326: Fazeli et al., in prep.). We present

[★] Based on observations with ESO-VLT, STS-Cologne GTO proposal ID 094.B-0009(A).

NIR IFS of the galaxy NGC 1672, which is a barred spiral galaxy (SB(r)bc). The classification of the nucleus has been challenging since the centre appears to be obscured by dust. Brandt et al. (1996) in ROSAT observations of the galaxy reported a soft diffuse X-ray source. de Naray et al. (2000) suggested that there is a Seyfert 2 in the centre, obscured by a Compton thick nucleus with a column density of at least 10^{24} cm^{-2} . Finally Jenkins et al. (2011) using the higher-resolution *Chandra* data, detected a hard X-ray nuclear source and conclude that the AGN is a low-luminosity Seyfert 2.

Jenkins et al. (2011) also studied the star-forming ring in NGC 1672 at a radius of $r \approx 5'' = 275 \text{ pc}$. Their observations show that the ring emits bright in the radio 3 cm data from the Australia Telescope Compact Array (ATCA), the *Spitzer* $8 \mu\text{m}$ band (tracing essentially the PAH dust), hard X-ray detected with *Chandra*, and $H\alpha$ and continuum emission in the optical spectra. The CO(3–2) emission line observed by ALMA shows high concentrations in the ILR ring (Combes et al. 2019).

The galaxy has a strong 2:4 bar with a position angle (PA) of 92° and four spiral arms (Baumgart & Peterson 1986). The inclination of the galaxy is low ($i = 34^\circ$; de Vaucouleurs et al. 1991), which makes it a good target for kinematical studies. However, as shown by previous studies, the kinematics at the centre of this galaxy seem to be very complex. Díaz et al. (1999), using the Multi-functional Integral Field Spectrograph (MIFiS) data studied the central 2 kpc, and Firpo et al. (2017), using the Gemini Multi-Object Spectrograph (GMOS) data studied the central $3''.5 \times 5''$. Both studies analysed the kinematics of the NGC 1672 by fitting the $H\alpha$ emission line profile. They both conclude that the nucleus is off centre with respect to the large-scale rotation disc. However, owing to the obscuration by dust and sensitivity of optical light to extinction, Firpo et al. (2017) suggested that NIR spectroscopy is needed to be certain. Díaz et al. (1999) also reported non-circular motions with an amplitude of $50\text{--}60 \text{ km s}^{-1}$.

According to Combes et al. (2019, from ALMA data) the kinematics of the CO(3–2) emission line reveals a typical S-shaped velocity pattern related to non-circular motions. Additionally they report thin filaments joining towards a central concentration, which they conclude to be a torus of radius $0''.5 = 27 \text{ pc}$ with decoupled kinematics from the large-scale disc.

Figure 1 shows an optical image of NGC 1672. The field of view (FOV) of the Spectrograph for INtegral Field Observations in the Near Infrared (SINFONI) data, which is analysed in detail in this paper, is indicated in red.

Throughout this paper, we adopt a luminosity distance of $D_L = 11.4 \text{ Mpc}$ which is the median value of the redshift-independent distances in NED (Steer et al. 2017). This corresponds to a scale of $55 \text{ pc arcsec}^{-1}$.

This paper is structured as follows: Sect. 2 presents the observation and data reduction. Section 3 contains the explanation of our analysis methods, shows the results we find, and gives a discussion and comparison to the literature. Section 4 summarises the results and the conclusions we draw from this study.

2. Observations and data reduction

NGC 1672 was observed on October 7, 2014 with the IFS SINFONI mounted at the Unit Telescope 4 (UT4; Yepun) of the ESO Very Large Telescope in Chile (VLT; Eisenhauer et al. 2003; Bonnet et al. 2004).

The observations were taken in seeing-limited mode, the FOV of single exposures in this mode is $8'' \times 8''$ and the spatial sampling is $0''.125 \text{ pixel}^{-1}$. Using a jitter pattern with offsets $\pm 1''$

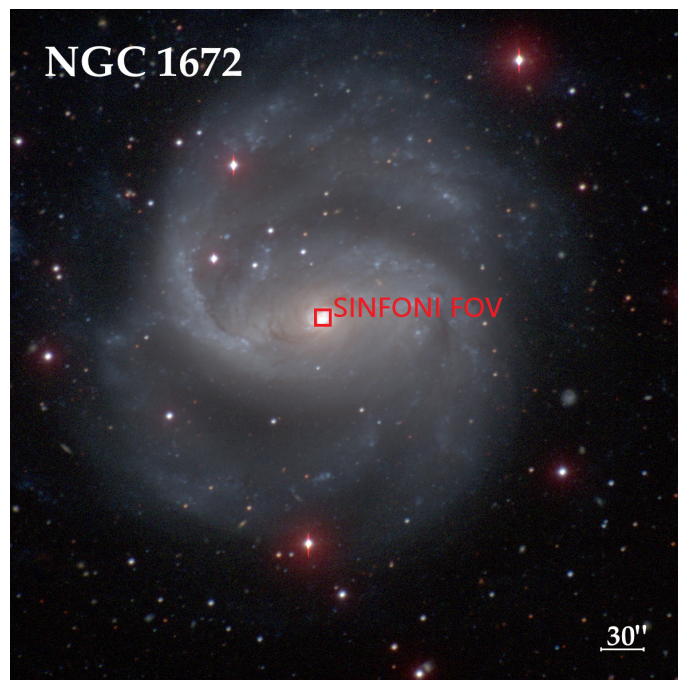


Fig. 1. Optical image of the spiral barred galaxy NGC 1672. The red box indicates the $10'' \times 10''$ ($550 \times 550 \text{ pc}^2$) SINFONI data. Image courtesy: Carnegie-Irvine Galaxy Survey (Ho et al. 2011).

we minimised the effect of bad pixels and increased the FOV of the combined cube to $10'' \times 10''$, which corresponds to a linear scale of 550 pc . We used gratings in the $H + K$ band with a spectral resolution of $R \approx 1500$ and in the K band with a resolution of $R \approx 4000$. We spent an integration time of 150 s per exposure. This leads to an overall on-source integration time of 1500 s ($10 \times 150 \text{ s}$) for the $H + K$ -grating and 3000 s ($20 \times 150 \text{ s}$) for the K -band grating, as well as an additional 750 s in $H + K$ -band and 1500 s in K band on-sky.

We used the ESO pipeline, up to single-exposure-cube reconstructions, for the data reduction. Initially some detector pattern features, which were imprinted in the SINFONI data, were corrected for (for more details see; Smajić et al. 2014) alignment, final coaddition, and telluric correction; our own PYTHON and IDL routines are used.

The G2V star HIP 039102 was observed in the $H + K$ and K bands as two object-sky pairs for each band, with an integration time of 1 s . The spectrum of this star was used to correct for atmospheric telluric absorption and for flux calibration. Prior to using the spectrum we eliminated the intrinsic spectral features and black-body shape of the standard star. This procedure was done using a high-resolution solar spectrum (Maiolino et al. 1996), which was convolved with a Gaussian to match the resolution of SINFONI. A black-body function with temperature $T = 5800 \text{ K}$ was used for the spectral region between the two bands and at the spectral edges to extrapolate the solar spectrum.

The flux calibration was performed by extracting a spectrum from the telluric standard star (aperture size = $3 \times FWHM_{\text{PSF}}$ Howell 2000). The full width at half maximum (FWHM) of the point spread function (PSF), measured by fitting a two-dimensional Gaussian to the telluric star, is $0''.5$. The calibration for standard star counts was done at $\lambda 2.1 \mu\text{m}$ for both the $H + K$ and K bands, to the flux taken from the 2MASS All-sky Point Source Catalogue (Skrutskie et al. 2006).

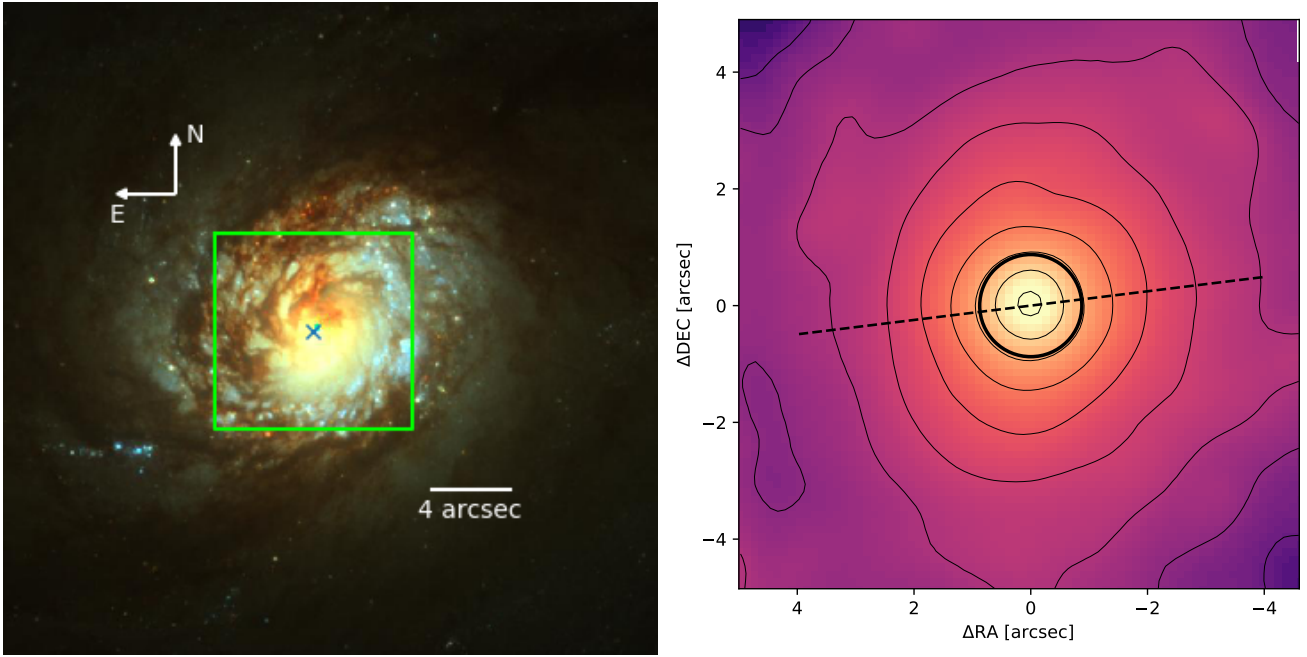


Fig. 2. *Left:* HST/ACS composite image of the central region of NGC 1672 (red: $F814W$, green: $F555W$, blue: $F435W$). The green box indicates the FOV of our SINFONI observations. *Right:* K -band continuum extracted from the SINFONI data cube, by taking the median of the spectrum around $\lambda \sim 2.15 \mu\text{m}$ (extracted from the $H + K$ data cube). The thicker black circle denotes the $FWHM \sim 1''.75$. The dashed line indicates the orientation of the large-scale bar.

3. Results and discussion

The most prominent feature in the central $10''$ of NGC 1672 is a nuclear ring that shows strong star-forming activity. Figure 2 (left) shows a composite image of the central region, where the FOV of SINFONI is overlaid in green. This image was obtained with the wide field channel (WFC) of the Advanced Camera for Surveys (ACS) instrument on-board the *Hubble* Space Telescope (HST) in broadband $F814W$, $F555W$ and $F435W$ filters¹. The star-forming ring becomes apparent in the blue channel. The emission seems to be asymmetric, which can be the result of obscuration by dust lanes from the north towards the east side of the ring.

Figure 2 (right) shows a K -band continuum image that was extracted from the reduced SINFONI data cube.

In the spectra of the galaxy extracted from the data cube, we identified several hydrogen recombination lines (e.g. $Pa\alpha$, $Br\gamma$ and $Br\delta$) and ro-vibrational molecular hydrogen lines ($H_2(1-0)S(3)$ $\lambda 1.96 \mu\text{m}$, $H_2(1-0)S(2)$ $\lambda 2.03 \mu\text{m}$, $H_2(1-0)S(1)$ $\lambda 2.122 \mu\text{m}$, $H_2(1-0)S(0)$ $\lambda 2.22 \mu\text{m}$ and $H_2(2-1)S(1)$ $\lambda 2.248 \mu\text{m}$), as well as the forbidden iron line $[\text{Fe II}]\lambda 1.644 \mu\text{m}$, He I , and many stellar absorption features. These lines are well-known tracers for physical conditions of different phases of the ISM. In the rest of this section we explain our analysis and results drawn from the SINFONI observations of the galaxy. In addition, we compare our results with the literature and discuss our findings.

3.1. Emission line fitting and flux distribution

To explore the distribution and kinematics of molecular and ionised (traced by hydrogen recombination lines here) gas in NGC 1672, we fit single Gaussian functions to the emission line

¹ Retrieved from the *Hubble* Legacy Archive (<http://hla.stsci.edu>). Observations took place on August 1, 2005, proposal ID 10354, PI: L. Jenkins.

profiles at each spatial pixel in the cube. To subtract the continuum baseline we fit a linear function to two spectral windows to the left and right of the emission line. For all line fits, we used the Levenberg-Marquardt algorithm as implemented in the Python library LMFIT (Markwardt 2009; Newville et al. 2014). Stated uncertainties correspond to the 1σ errors derived from the covariance matrix.

The forbidden iron-transition $[\text{Fe II}]\lambda 1.644 \mu\text{m}$ in the H band is slightly blended by the stellar absorption feature $\text{CO}(7-4)$ $\lambda 1.641 \mu\text{m}$. Therefore, before fitting the line we subtracted the stellar absorption features, using the PYTHON implementation of the penalized pixel-fitting method² (Cappellari & Emsellem 2004; Cappellari 2017) with default parameters.

We used a set of synthetic model spectra from Lançon et al. (2007), which have assumed solar abundances, gravities of $\log(g/\text{cm s}^{-2}) = [-1, -0.5, 0, +1]$, cover an effective temperature range of $T_{\text{eff}} = 2900\text{--}5900 \text{ K}$, and have masses of $1 M_{\odot}$ and $15 M_{\odot}$; red giants and supergiants which are representative of the intermediate-to-old stellar populations in the bulge. The model spectra were convolved with a Gaussian kernel to match the spectral resolution of our observation. To reach the necessary signal-to-noise ratio, prior to fitting the stellar absorption features, we spatially smoothed the SINFONI data cube with a three-pixel boxcar filter.

Maps of the emission line flux distributions of the lines that have the strongest emission, $Br\gamma$, $H_2\lambda 2.122 \mu\text{m}$, $[\text{Fe II}]\lambda 1.644 \mu\text{m}$, and He I are shown in Fig. 3. The maps are clipped to have uncertainties in the emission line flux of less than 30%. In the maps we denote the position of the nucleus, that is where the continuum emission around $2.2 \mu\text{m}$ peaks, with an N.

In all the line flux maps we detect emission from hot spots in the ILR star-forming ring. Especially, the emission is asymmetric and stronger in south-east to west side and lower in the

² www-astro.physics.ox.ac.uk/~mxc/software/PPXF version (V6.7.8).

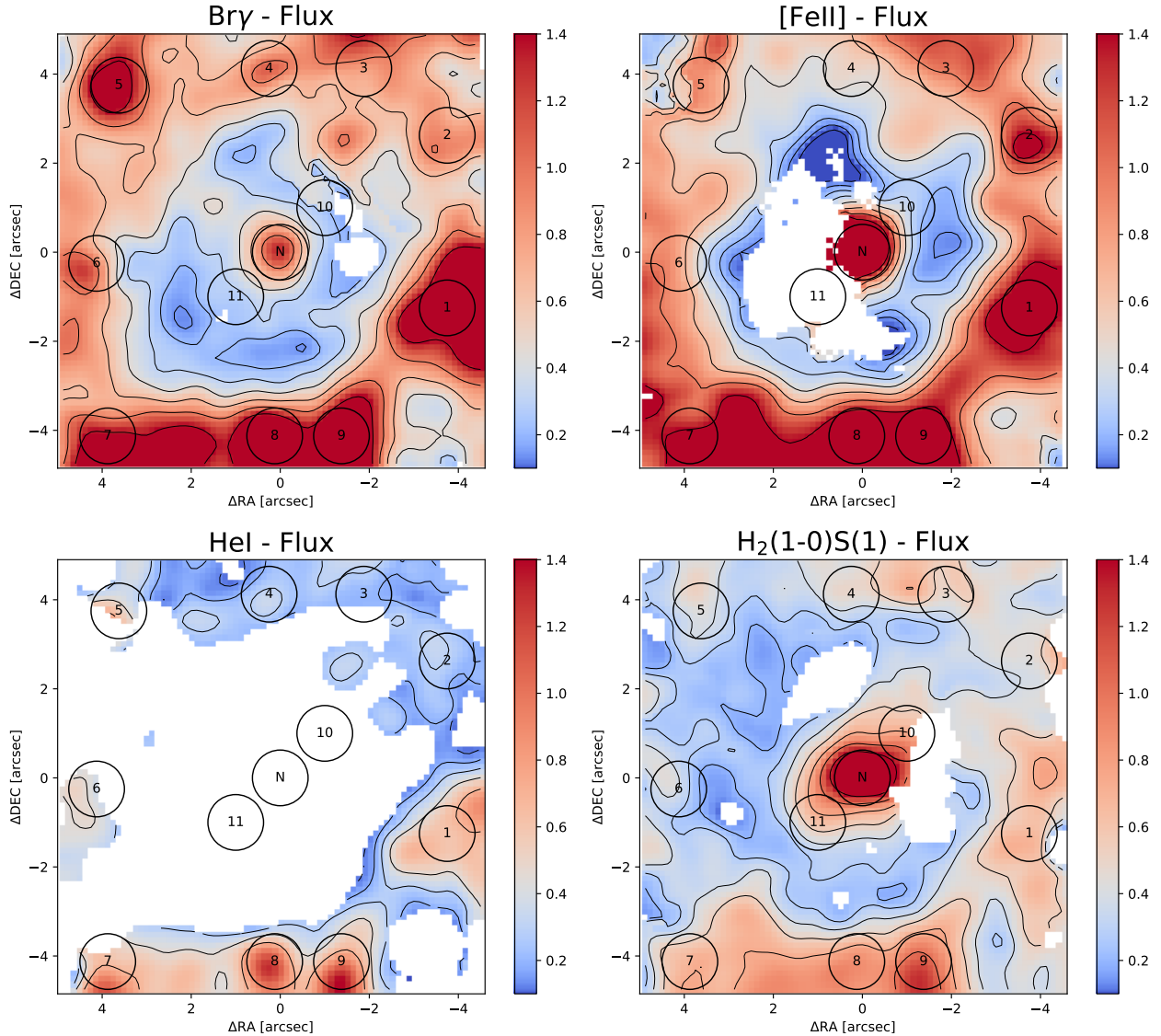


Fig. 3. Results of emission line fitting for the inner region of NGC 1672 using a single Gaussian component. *From top left to bottom right:* flux maps of $\text{Br}\gamma$ $\lambda 2.166\ \mu\text{m}$, $[\text{Fe II}]\ \lambda 1.644\ \mu\text{m}$, $\text{H}_2\ \lambda 2.12\ \mu\text{m}$, and He I emission lines. In all of the maps the flux units are $10^{-20}\ \text{W m}^{-2}$. All spatial pixels for which the uncertainty of the emission line fit is higher than 30% are clipped. These pixels are shown in white. North is up and east is to the left.

east and north-west side of the ring. At the centre the molecular gas shows extended emission. On the contrary, the emission of $[\text{Fe II}]$ and $\text{Br}\gamma$ have a very concentrated emission only in the nucleus region only (denoted by N).

We set several apertures with size $r \sim 0''.625$ (5 pixels), at regions where the emission is stronger, to study their excitation mechanisms in more detail. The positions are tabulated in Table 1 and indicated in the flux maps in Fig. 3. The corresponding spectra are shown in Fig. 4. The stellar continuum emission was fitted, using PPXF as described above. The fitted continuum spectra are indicated in blue (Fig. 4).

3.2. Extinction correction

The extinction effect by dust is lower in the NIR compared to the optical, however not negligible. Extinction is often estimated by comparing the line ratios of two hydrogen recombination lines as predicted by models with those observed. It is then assumed that the deviation of the observed line ratio from the predicted line is

solely caused by external extinction. However, this is only feasible when accurate line measurements are available throughout the FOV. We decided not to use the emission line ratios as $\text{Pa}\alpha$ and $\text{Br}\delta$ lines both lie in a region where atmospheric effects produce significant noise contribution. Therefore we used the $H - K$ colour map to estimate the extinction. A $H - K$ colour map is shown in Fig. 5.

In order to convert the $H - K$ colour to visual extinction A_V we used the following relation from Teixeira & Emerson (1999):

$$A_V = k E(H - K) = k [(H - K) - (H - K)_0], \quad (1)$$

and employed the Calzetti et al. (2000) attenuation law for Galactic diffuse ISM ($R_V = 3.12$). This corresponds to a factor of $k = 14.6$.

The unreddened intrinsic colour of a typical quiescent galaxy is $(H - K)_0$. We use $(H - K)_0 = 0.22$ (Glass 1984). It is assumed that the stellar populations within the FOV, or to be accurate, their intrinsic $H - K$ colours do not vary intrinsically but changes

Table 1. Coordinates, H - and K -band flux densities, $H - K$ colour, and extinction calculated from the $H - K$ colour for the apertures in the ILR ring and at the centre of NGC 1672.

Aperture	(X-offset, Y-offset) [arcsec, arcsec]	H -band $10^{-15} \text{ W m}^{-2} \mu\text{m}^{-1}$	K -band $10^{-15} \text{ W m}^{-2} \mu\text{m}^{-1}$	$H - K$ [mag]	A_V [mag]
N	(0.0, 0.0)	14.53	9.21	0.56	5.0
1	(-3.75, -1.25)	2.33	1.38	0.49	3.9
2	(-3.75, 2.625)	2.17	1.26	0.47	3.6
3	(-1.875, 4.125)	2.24	1.3	0.46	3.5
4	(0.25, 4.125)	2.02	1.2	0.49	3.9
5	(3.625, 3.75)	1.64	0.97	0.48	3.8
6	(4.125, -0.25)	1.79	1.08	0.51	4.2
7	(3.875, -4.125)	1.65	1.05	0.56	5.0
8	(0.125, -4.125)	2.39	1.46	0.52	4.4
9	(-1.375, -4.125)	1.95	1.22	0.55	4.8
10	(-1.0, 1.0)	6.46	3.76	0.47	3.6
11	(1.0, -1.0)	6.42	3.7	0.46	3.5

Notes. The H - and K -band flux densities are extracted from the $H + K$ data cube by taking a median of the spectrum around $\lambda \sim 1.6 \mu\text{m}$ and $\lambda \sim 2.15 \mu\text{m}$, respectively.

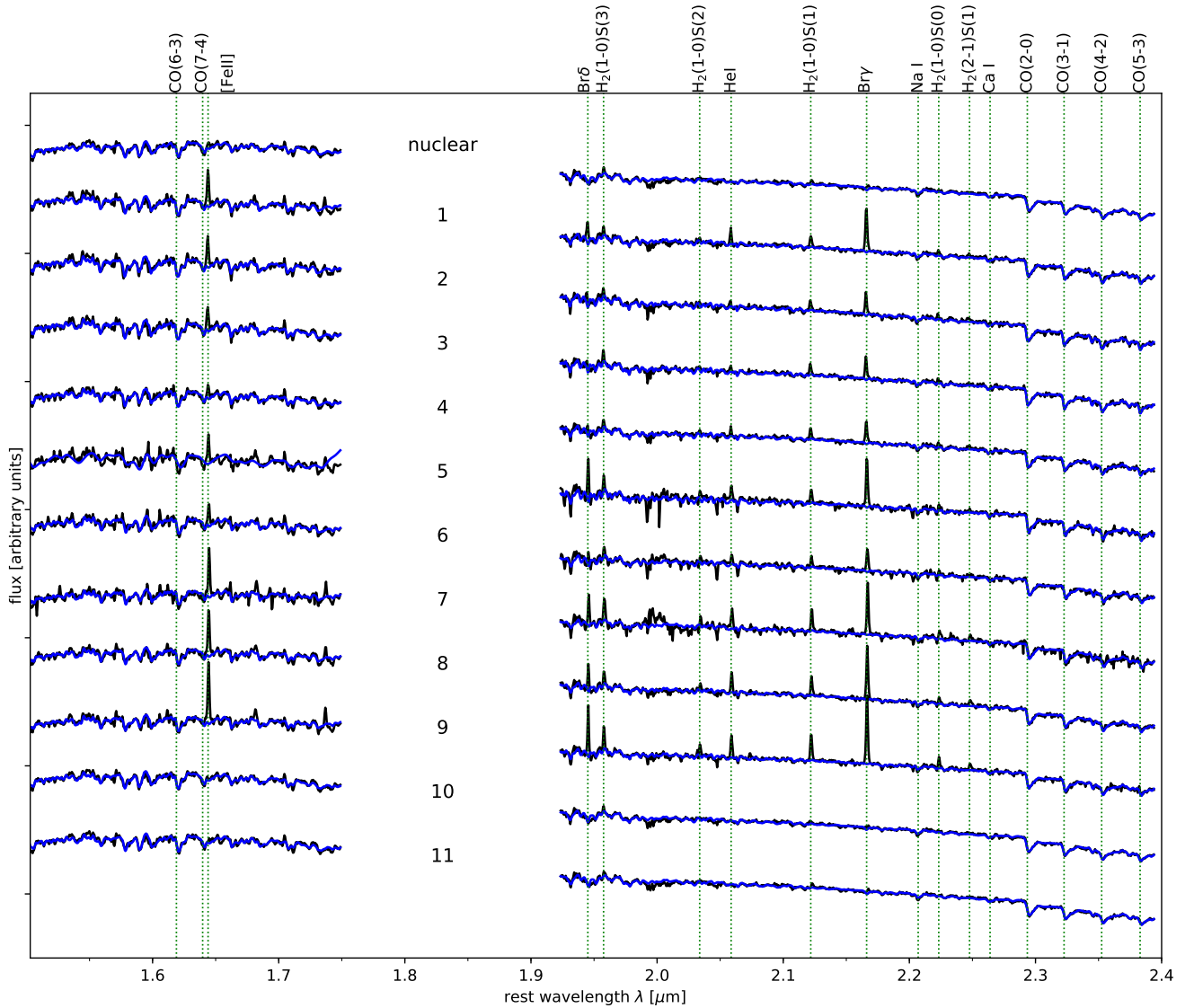


Fig. 4. Normalised spectra of the nuclear region and 11 apertures in the ILR ring and inside-the-ring regions. The positions at which the apertures are extracted are indicated in Fig. 3. Several emission and absorption lines are indicated with green vertical lines. The stellar continuum fit is shown in blue.

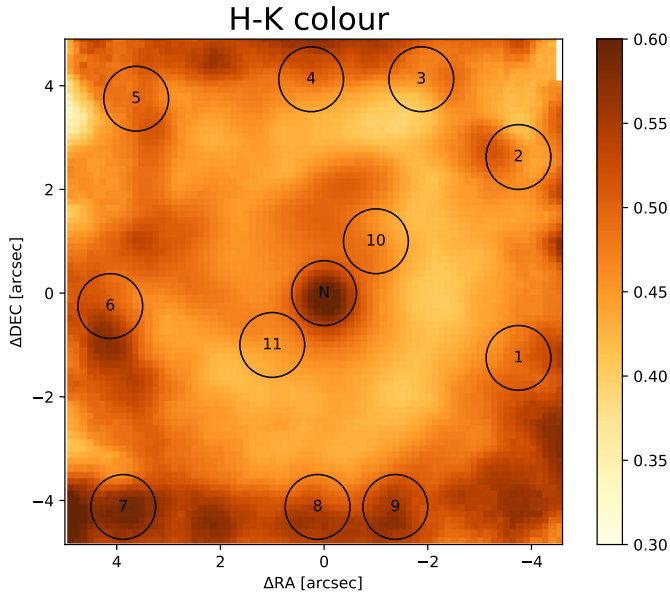


Fig. 5. Colour map for $H - K$ bands. North is up and east is to the left.

in the colour are caused by extinction only. Given that we see a star-forming ring with population ages of a few Myrs, this is probably not completely accurate. Stellar population models predict, depending on their set-up, a range from $(H - K)_0 = 0.1$ to $(H - K)_0 = 0.4$ mag for these populations (and references therein Grosbøl & Dottori 2012).

For typical colours of $(H - K) \approx 0.55$ in the ring, this leads to an A_V range from ~ 2.2 (high $(H - K)_0$) to ~ 6.5 (low $(H - K)_0$), which means that in the case of higher $(H - K)_0$ we tend to overestimate the flux by $\sim 20\%$ and in the case of lower $(H - K)_0$ we tend to underestimate the intrinsic flux by $\sim 20\%$ when applying our correction.

Emission lines are also fitted in the apertures, following the stellar continuum subtraction (as described in Sect. 3.1). However, for the Bry emission line in the nuclear aperture the stellar continuum fit produced an artificial effect, therefore we leave the stellar feature on the left side of this emission line as it is. The flux values, corrected for extinction (except for the nuclear aperture due to AGN contamination), for molecular gas are tabulated in Table 2, while the fluxes for ionised gas can be found in Table 3.

3.3. Gas excitation

In this section we assess the dominant mechanisms that excite the gas in different regions of the FOV. To do that, we use diagnostic line ratios. This means, we analyse the line ratios between lines that are excited by different excitation mechanisms to different amounts. In our investigation, we use the line ratio of the molecular hydrogen line $H_2\lambda 2.12\mu\text{m}$, the forbidden iron line [Fe II] to the hydrogen recombination line Bry, as well as between different species of H_2 emission lines (Figs. 6 and 7). Line-ratio diagrams suggest certain thresholds and demarcations to separate between excitation mechanisms such as AGN photo-ionisation or UV ionisation by photons produced in, for example starburst regions. Since the lines [Fe II] and Bry are located in two different bands (H and K -band) and have therefore a significant separation in wavelength, extinction can have a significant impact. We therefore use extinction-corrected line fluxes that are also in accordance with the literature.

The diagram in Fig. 6 uses the previous studies from Riffel et al. (2013a) and Colina et al. (2015) to set demarcation between young starburst, older supernova remnant, and AGN-dominated regions. The results show a clear deviation among ILR, central and nucleus apertures. The ILR apertures (1–9) mainly lie in young starburst-dominated regions. The nucleus and central apertures (10, 11) show more signs of AGN- and supernovae-dominated regions.

In Fig. 7 we display the $H_2(1-0)S(3)/H_2(1-0)S(1)$ versus $H_2(2-1)S(1)/H_2(1-0)S(1)$ line ratios. Molecular hydrogen can be excited by a variety of mechanisms as follows: thermal processes, in which shocks (Hollenbach & McKee 1989) collisionally excite the gas; X-ray (Maloney et al. 1996) radiation from, for example the AGN that heats up the gas; and non-thermal processes, i.e. UV fluorescence mechanisms, in which UV photons from for example OB stars or strong AGN continuum emission excite the H_2 molecules (Black & van Dishoeck 1987). The diagram shows that in most of the apertures a combination of those excitation mechanisms is responsible for the gas excitation. However the line ratios of the nucleus imply a higher contribution of thermal and shock excitation mechanisms.

The significant contribution of non-thermal excitation that we see in the apertures in the ring is typical for star-forming regions (e.g. Rodríguez-Ardila et al. 2005; Busch et al. 2017; Fazeli et al. 2019). This underlines that the ring is dominated by star formation. The excitation of the nucleus is less clear. The observed line ratios could be caused by an (ageing) starburst but also by a (weak) AGN.

3.4. Molecular and ionised gas masses

We estimate the total hot molecular gas mass using the extinction-corrected H_2 1–0S(1) emission line (Scoville et al. 1982; Wolniewicz et al. 1998).

$$M_{H_2} = 5.0776 \times 10^{16} \left(\frac{D_L}{\text{Mpc}} \right)^2 \left(\frac{F_{H_2 1-0S(1)}}{\text{W m}^{-2}} \right) M_{\odot}. \quad (2)$$

In this equation $D_L = 11.4$ Mpc is the luminosity distance of the galaxy and we assume that the gas is in local thermal equilibrium and has a typical vibrational temperature of $T_{\text{vib}} = 2000$ K (for better comparison with the literature where this value is most often chosen). It is important to mention that this assumption is not completely accurate and can lead to an overestimation of the hot molecular gas mass up to a factor of 2 (Busch et al. 2017). However for better comparison of our results with the literature values we follow this assumption.

We find a total hot molecular gas mass of $260 M_{\odot}$ in the $10'' \times 10''$ SINFONI FOV. This value only represents the hot surface of molecular gas clouds. To estimate the corresponding cold molecular gas mass we employ the conversion factor: $M_{H_2(\text{cold})}/M_{H_2(\text{hot})} = (0.3-1.6) \times 10^6 M_{\odot}$ from Mazzalay et al. (2013), which leads to $(0.8-4.1) \times 10^8 M_{\odot}$ cold molecular gas. The dispersion observed in the CO-to- H_2 conversion factor is due to the variety of galaxy types that were used to measure this relation and the intrinsic regularities of the distribution of gas in these galaxies. The CO(3–2) flux integrated over a $10'' \times 10''$ aperture is $S_{\text{CO}} \Delta\nu = 465 \text{ Jy km s}^{-1}$ (ALMA project ID 2015.1.00404.S, PI F. Combes). Using a Milky Way-like galaxy CO-to- H_2 conversion factor (CO(3–2)/CO(1–0) ~ 0.8 and $\alpha_{\text{CO}} \sim 4.36$) this results in $M_{H_2(\text{cold})} = 0.9 \times 10^8 M_{\odot}$ (F. Combes, priv. comm.), which is in good agreement with our estimated cold gas mass.

Table 2. Molecular hydrogen emission lines in the apertures in the ILR ring, nucleus, and within-the-ring regions, and derived quantities for hot and cold molecular gas masses.

Aperture	H ₂ (1–0)S(3) λ1.958 μm	H ₂ (1–0)S(2) λ2.034 μm	H ₂ (1–0)S(1) λ2.122 μm	H ₂ (1–0)S(0) λ2.223 μm	H ₂ (2–1)S(1) λ2.248 μm	Hot H ₂ mass [M _⊙]	Cold gas mass [10 ⁶ M _⊙]
N	18.97 ± 5.16	22.91 ± 5.42	22.30 ± 4.72	4.36 ± 2.84	3.35 ± 1.92	25	8–40
1	3.25 ± 0.77	3.08 ± 0.64	6.55 ± 0.49	2.65 ± 0.40	1.67 ± 0.28	7	2–12
2	2.51 ± 0.74	2.35 ± 0.66	4.98 ± 0.62	2.14 ± 0.36	1.74 ± 0.33	6	2–9
3	4.52 ± 0.55	2.30 ± 0.51	5.29 ± 0.41	1.83 ± 0.32	1.08 ± 0.33	6	2–10
4	2.94 ± 0.44	2.34 ± 0.49	4.86 ± 0.37	1.74 ± 0.33	1.49 ± 0.27	5	2–9
5	4.76 ± 0.50	3.02 ± 0.86	4.30 ± 0.44	1.74 ± 0.38	0.91 ± 0.21	5	1–8
6	3.43 ± 0.55	3.12 ± 0.89	3.63 ± 0.50	1.36 ± 0.42	0.87 ± 0.36	4	1–7
7	9.52 ± 0.62	4.89 ± 0.95	8.36 ± 0.42	2.78 ± 0.43	2.17 ± 0.42	9	3–15
8	6.76 ± 0.64	4.52 ± 0.66	9.50 ± 0.53	3.05 ± 0.36	3.04 ± 0.36	11	3–17
9	10.67 ± 0.69	6.01 ± 0.77	12.44 ± 0.37	4.43 ± 0.38	2.85 ± 0.29	14	4–22
10	5.99 ± 1.95	7.82 ± 2.05	7.74 ± 1.69	–	1.70 ± 0.75	9	3–14
11	4.72 ± 1.29	5.62 ± 1.51	5.48 ± 1.15	0.99 ± 0.70	1.04 ± 0.56	6	2–10

Notes. The flux units are 10^{−19} W m^{−2}. Nuclear aperture flux values are not corrected for extinction as their $H - K$ colour might be contaminated by the central source.

Table 3. Emission line fluxes for the apertures and derived quantities ionised gas mass and star formation rate.

Aperture	[Fe II] λ1.644 μm	Paα λ1.876 μm	Brδ λ1.945 μm	He I λ2.059 μm	Bry λ2.166 μm	H II mass [10 ⁴ M _⊙]	SFR [10 ^{−3} M _⊙ yr ^{−1}]
N (*)	18 ± 4	–	–	–	8 ± 2	5.2	13
1	16.0 ± 1.2	90.9 ± 1.8	3.9 ± 1.0	2.5 ± 0.5	10.3 ± 0.6	6.6	17
2	9.1 ± 1.1	75.4 ± 1.9	4.2 ± 1.0	3.6 ± 0.5	10.1 ± 0.6	6.5	17
3	16.6 ± 1.4	27.2 ± 2.3	13.1 ± 1.3	4.6 ± 0.9	17.1 ± 0.6	11.0	29
4	14.0 ± 1.3	37.8 ± 2.0	3.8 ± 1.3	4.2 ± 1.1	9.5 ± 0.7	6.1	16
5	30.5 ± 1.5	160.6 ± 2.9	12.0 ± 1.1	8.2 ± 0.9	19.6 ± 0.9	12.6	33
6	38.6 ± 1.7	82.0 ± 2.7	13.7 ± 1.3	11.3 ± 0.6	27.9 ± 0.9	17.9	47
7	44.8 ± 1.7	43.5 ± 2.6	21.8 ± 1.2	10.5 ± 0.7	31.0 ± 1.1	19.9	52
8	10.2 ± 5.0 ⁽⁺⁾	39.0 ± 5.1	0.8 ± 0.0	6.2 ± 1.3	7.1 ± 1.5	4.6	12
9	16.7 ± 4.7	18.0 ± 4.1	2.5 ± 2.6	3.6 ± 1.0	7.3 ± 1.2	4.7	12
10	10.2 ± 5.0 ⁽⁺⁾	–	–	–	7.1 ± 1.5	3.3	9
11	–	–	–	–	7.4 ± 1.2	2.2	6

Notes. The flux units are 10^{−19} W m^{−2}. (*)For the nuclear aperture we reported the extinction value in Table 1, however, the flux values for this aperture are not corrected for extinction because of AGN contamination of $H - K$ -colour. (+)The emission line fit values have uncertainties higher than 30%. However, the emission line fit reveals a line, therefore we report the flux in the table.

Furthermore, we estimate the mass of ionised gas using the extinction corrected flux of the Bry emission line (assuming case B recombination, Osterbrock 1989) as follows:

$$M_{\text{H II}} \approx 2.9 \times 10^{22} \left(\frac{f_{\text{Bry}}}{\text{W m}^{-2}} \right) \left(\frac{D_{\text{L}}}{\text{Mpc}} \right)^2 \left(\frac{n_{\text{e}}}{\text{cm}^{-3}} \right)^{-1} M_{\odot}. \quad (3)$$

We assume a temperature of $T = 10^4$ K and electron density of $n_{\text{e}} = 10^2 \text{ cm}^{-3}$. We find the total ionised gas mass in the SINFONI FOV to be $\approx 2.3 \times 10^6 M_{\odot}$.

We also report the estimated gas masses of the ionised and molecular (hot and cold) in the respective apertures. The results are listed in Tables 2 and 3.

Literature comparison. Using the H α emission line flux of a 4'' diameter aperture drawn from the Siding Spring Southern Seyfert Spectroscopic Snapshot Survey (S7; for more details about data release; Thomas et al. 2017; Dopita et al. 2015) observed by the Wide Field Spectrograph (WiFeS) on ANU

2.3 m telescope at the Siding Spring Observatory, a flux value of $1.2 \times 10^{-16} \text{ W m}^{-2}$ is reported. We estimate an ionised gas mass of $\approx 4.5 \times 10^5$, which is consistent with our results (for a comparable aperture we get $\approx 2 \times 10^5$) for the ionised gas mass.

Typical gas masses in the central kiloparsec of nearby galaxies, found by the AGNIFS group (Riffel et al. 2016, and references therein) and our group are of the order of $10 < M_{\text{H}_2} < 10^3 M_{\odot}$ (hot molecular gas) and $10^4 < M_{\text{H II}} < 10^7 M_{\odot}$ (ionised gas). Typical cold molecular gas masses, from CO observations, for nearby galaxies, are $10^8 < M_{\text{H}_2} < 10^{10} M_{\odot}$ (Moser et al. 2012, and references therein). In that sense, NGC 1672 has very typical gas masses for nearby galaxies. The ratio of mass of ionised gas to hot molecular gas is $M_{\text{H II}}/M_{\text{H}_2} \approx 8900$, which is at the upper end of ratios but still typical for nearby galaxies (Fazeli et al. 2019, case of NGC 1365 and references therein). Similar to NGC 1365, the high ratio could be caused by additional ionised gas excitation in the centre from a (weak) AGN (see Sect. 3.7 herein further discussion).

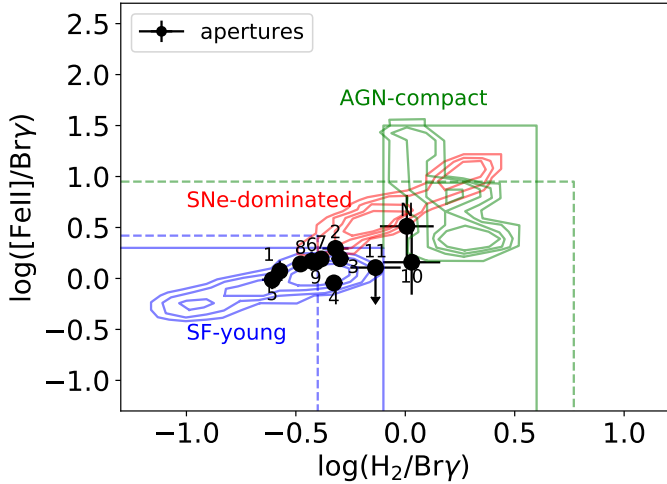


Fig. 6. Diagnostic diagram of the apertures in the central kiloparsec of NGC 1672. The locations of the apertures are indicated in the flux maps in Fig. 3. The flux ratios of the $H_2(1-0)S(1)\lambda 2.122\ \mu\text{m}/B_{\text{Bry}}$ and $[\text{Fe II}]\lambda 1.644\ \mu\text{m}/B_{\text{Bry}}$ emission lines are used. The contours show the demarcation for young star formation, supernovae, and compact AGN; the solid lines denote upper limits for young star formation and AGN, both from Colina et al. (2015), derived using IFS data. The dashed lines denote upper limits for star formation and AGN activity (derived from slit-spectroscopy; Riffel et al. 2013b). An upper limit value for the $[\text{Fe II}]$ flux was calculated for aperture 11.

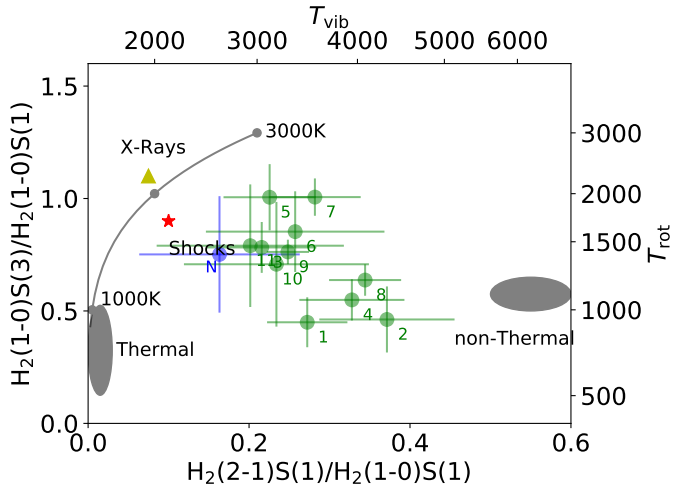


Fig. 7. Diagnostic diagram of the apertures in the central kiloparsec of NGC 1672. The location of the apertures is indicated in the flux maps in Fig. 3. The flux ratios of the molecular hydrogen lines $H_2(2-1)S(1)\lambda 2.248\ \mu\text{m}/H_2(1-0)S(1)\lambda 2.122\ \mu\text{m}$ and $H_2(1-0)S(3)\lambda 2.034\ \mu\text{m}/H_2(1-0)S(0)\lambda 2.223\ \mu\text{m}$ are used (Mouri 1994; Rodríguez-Ardila et al. 2004, 2005). Models for thermal UV excitation (Sternberg & Dalgarno 1989), non-thermal excitation (Black & van Dishoeck 1987), X-ray heating (Draine & Woods 1990), and shock-heating (Brand et al. 1989) are indicated for comparison.

3.5. Stellar and gaseous kinematics

3.5.1. Stellar kinematics

In this section, we analyse the stellar kinematics that are traced by the CO absorption band heads at the red end of the K band; the CO(2-0) absorption band head at a rest-frame wavelength of $2.29\ \mu\text{m}$ is most prominent.

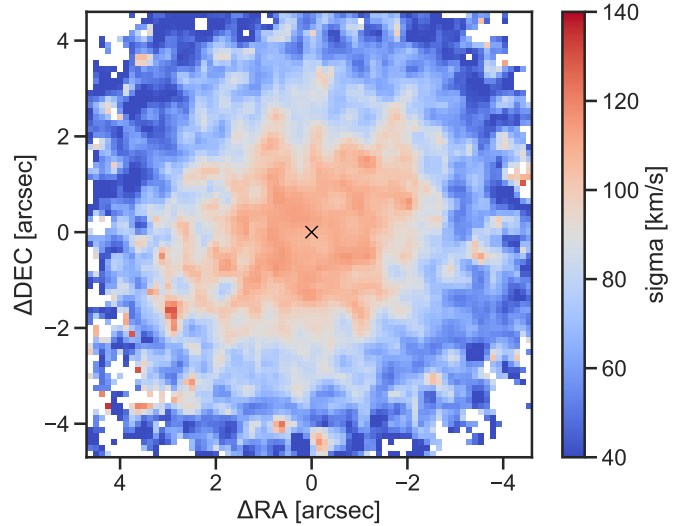


Fig. 8. Stellar velocity dispersion. North is up and east is to the left. The black cross denotes the nucleus.

We used the PPXF method (Cappellari & Emsellem 2004; Cappellari 2017) with default parameters to model the stellar continuum in a spectral window between $2.28\ \mu\text{m}$ and $2.42\ \mu\text{m}$. As spectral templates, we use the Gemini library of late spectral templates (Winge et al. 2009). The 29 stars with spectral classes of F7 to M5 are selected to suit as stellar templates for velocity dispersion measurement studies in the NIR like this work. Convolution with a Gaussian function in the spectral axis was used to bring the templates to the same spectral resolution as the SINFONI spectra. In the spatial dimensions, we use a boxcar filter of three pixels in diameter to reach the necessary signal to noise of ≈ 50 .

Stellar velocity dispersion. In Fig. 8, we show the map of the stellar velocity dispersion. In the centre, the velocity dispersion reaches values of $105\text{--}115\ \text{km s}^{-1}$. This is consistent with the HyperLEDA value of $109.5\ \text{km s}^{-1}$ (based on measurements of Garcia-Rissmann et al. 2005). Towards the edges of the FOV, the stellar velocity dispersion decreases significantly. Centrally peaked velocity dispersion profiles are often observed in classical bulges, while the profiles in pseudo-bulges are flatter (Fabricius et al. 2012). However, since the drop is most prominent at the location of the ring, star formation can also be an explanation for the lower velocity dispersions. Star formation regions are often observed to show a lower stellar velocity dispersion, which is explained by the stars still resembling the dynamics of the cold molecular gas from which they emerged (e.g. Riffel et al. 2011; Mazzalay et al. 2014; Busch et al. 2017). However, since the ring is located at the edge of our FOV and we cannot measure the stellar velocity dispersion outside of the ring towards larger radii, we cannot decide whether we see a drop due to the star-forming ring or just the transition between bulge and disc.

Stellar line-of-sight velocity. The stellar line-of-sight velocity (LOSVD) that we map in Fig. 9 (left) shows a very regular disc rotation with blueshifts in the north-west and redshifts in the south-east. The velocity amplitude within our FOV reaches about $100\ \text{km s}^{-1}$.

In order to quantify this finding, we fit a model to the observed LOSVD field. We assume that the stars follow Keplerian orbits in the gravitational potential of the stellar bulge and that it can be described by a Plummer function. In this case, the

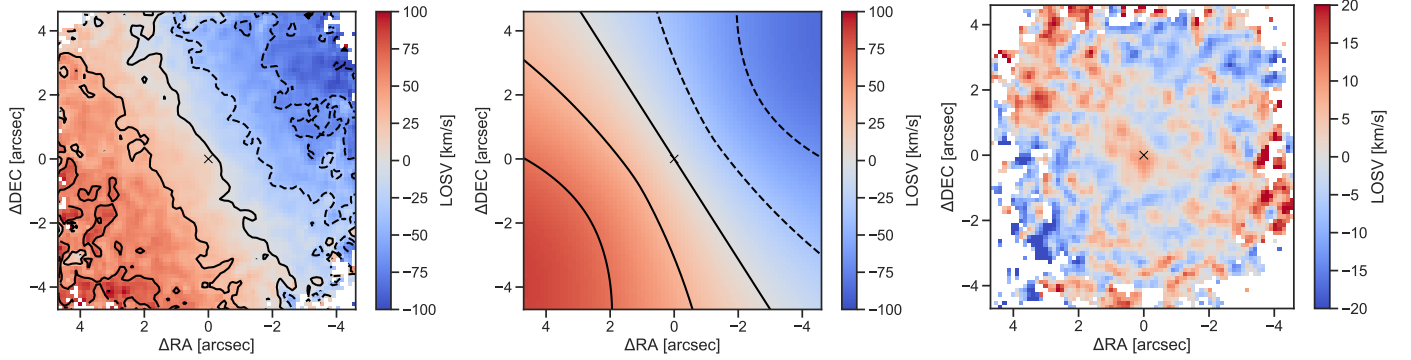


Fig. 9. *Left:* stellar velocity field map derived from fitting the spectral region around the CO(2–0) band head at $\sim 2.29 \mu\text{m}$. *Middle:* model of the LOSV, assuming circular motions in a Plummer gravitational potential. *Right:* residuals after subtracting the model from the observed LOSV field. The systemic velocity derived in the model fit is subtracted from the maps. North is up and east is to the left.

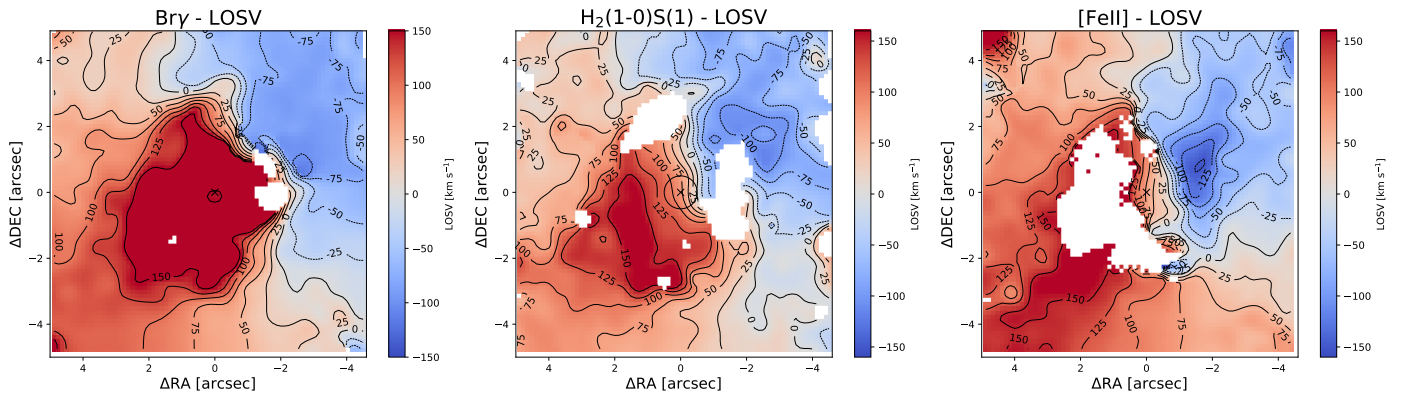


Fig. 10. Gas velocity fields, results of fitting $\text{Br}\gamma$, $\text{H}_2(1-0)\text{S}(1)\lambda 2.122 \mu\text{m}$, and $[\text{Fe II}]\lambda 1.644 \mu\text{m}$ emission lines. The black cross denotes the nucleus, where the continuum flux peaks. The circle in the H_2 map indicates the central arcsec where Combes et al. (2019) found a molecular torus. All velocities are given relative to the systemic velocity of 1392 km s^{-1} . North is up and east is to the left.

radial velocity is given by

$$v_r = v_s + \sqrt{\frac{R^2 GM}{(R^2 + A^2)^{3/2}}} \frac{\sin(i) \cos(\Psi - \Psi_0)}{\left[\cos^2(\Psi - \Psi_0) + \frac{\sin^2(\Psi - \Psi_0)}{\cos^2(i)} \right]^{3/4}}, \quad (4)$$

where G is the gravitational constant, R and Ψ are cylindrical coordinates, A is the scale length and M is the mass of the bulge, i is the inclination, and Ψ_0 is the position angle of the line of nodes. The inclination was fixed to the inclination given in HyperLEDA (Makarov et al. 2014) of $i = 29^\circ$. Further, we fixed the central position to the position of the peak of the K -band continuum emission. Our fit then results in a systemic velocity of $v_s = (1392 \pm 1) \text{ km s}^{-1}$ (after heliocentric correction) and a position angle of the line of nodes of $\Psi_0 = (302.5 \pm 0.9)^\circ$.

Figure 9 (middle panel) shows a map of the modelled LOSV. The residuals after subtracting the model from the observed LOSV, are shown in the right panel of Fig. 9. We do not see any systematic, only stochastic residuals with a rather low amplitude of $\lesssim 20 \text{ km s}^{-1}$, which indicates a good match between observed velocity field and model.

3.5.2. Gas kinematics

The fit routine that we use in Sect. 3.1 to derive the emission line flux distributions also provides central positions and widths of the emission line fits, from which we derive the LOSV and velocity dispersion (σ). Velocity field maps of $\text{Br}\gamma$, $[\text{Fe II}]$,

and $\text{H}_2(1-0)\text{S}(1)$ are shown in Fig. 10. White pixels correspond to clipped areas, using the same criteria as for the emission line maps. The velocities are shown relative to the systemic velocity 1392 km s^{-1} , derived from the stellar velocity model (Sect. 3.5.1).

Comparison of stellar and gas velocity maps. On first sight all the gas velocity field maps show signs of circular rotation, similar to the stellar velocity field, blue-shifted in the north-west and red-shifted in the south-east. However the gas velocities show higher amplitudes than stellar velocities. This could be because most of the kinetic energy of the stars go into random motion, contrary to the molecular gas that has lower velocity dispersion and therefore is more confined to the galaxy plane. Also unlike the stellar velocity field, which is fairly regular and can be fitted by a rotational model very well, leaving only stochastic residuals, the gas velocity fields show significant deviations from pure rotation. In particular, the twisted zero-velocity contours (Fig. 10), especially in molecular gas where the emission line has high signal-to-noise ratio in the centre (see Fig. 11, middle), are witnessing the presence of non-circular motions. A twisted zero-line velocity in (cold) molecular gas velocity fields has also been revealed by Combes et al. (2019, S-shaped zero-velocity in their Fig. 11) from their sub-millimetre CO(3–2) transition molecular gas velocity map.

Molecular and ionised gas. Zooming in to the central arc-second of the $\text{H}_2(1-0)\text{S}(1)$ and $[\text{Fe II}]$ velocity maps (denoted with a circle in Fig. 10, middle), we observe a shift in the

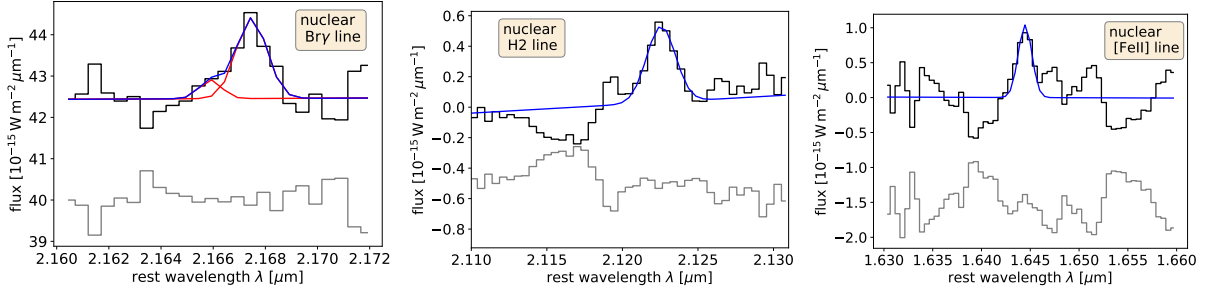


Fig. 11. From left to right: Br γ , H $_2$ (1–0)S(1) λ 2.122 μ m, and [Fe II] emission line fits detected in the nuclear aperture of radius 0.625. The original spectra are shown in black, the fitted model in blue, and the residuals are shown in grey. For the Br γ emission line a double-Gaussian fit is used as explained in Sect. 3.5.2. The stellar continuum is not subtracted in the spectra shown.

PA of the zero-velocity line from $\sim 35^\circ$ of the large scale rotation to $\sim 0^\circ$. This most probably reflects the circumnuclear disc observed by Combes et al. (2019) in CO(3–2). This structure which they call the molecular torus has a position angle of the zero-velocity line of 0° and an inclination of 64° and is therefore dynamically decoupled from the large-scale disc. However, since its size of 0.5 is of the order of our spatial resolution, we cannot resolve more details with our data.

Position of the kinematical centre. Furthermore, the gas velocity gradients in the centre are very steep and the centre of the velocity field seems to be (about 0.5 in H $_2$ and 1'' in Br γ LOSV maps) shifted to north-west compared of the centre, where the K -band continuum and narrow emission lines peak. As mentioned in the introduction, Díaz et al. (1999) and Firpo et al. (2017) reported an offset of 60 pc (0.8 considering the distance they adopt), studying kinematics of H α emission line.

A gas kinematic centre offset from the nucleus has also been suggested for the Milky Way by Blitz (1994). In the Galactic scenario, this author proposed that the shallow gravitational potential towards the centre can result in the gas being less strongly bound to the nuclear stellar bulge region. In this shallow potential the gas can then slosh around the nuclear position. As a result the kinematic centre may be observed as being offset from the stellar and AGN centre. However, in NGC 1672 there is even a gap between the hot molecular and the ionised gas kinematics centre.

The presence of an outflow is another mechanism that might induce an offset in the kinematics centre of the gas. However, we rule out this scenario for NGC 1672 as we discuss in the following.

Double-component hydrogen recombination lines. Investigating the spectra of the galaxy in the centre we recognise that the Br γ and Pa α emission line profiles at the nucleus and the regions north and north-west of the nucleus show a second component or double-horned profile. We display these emission line fits and the position of the apertures they were extracted from on the Br γ flux map in Fig. 12 (left).

In the top panel of Fig. 12 we present the flux map of the emission line H α λ 6562.8 with a FOV of $38'' \times 25''$ and pixel size 1''. The data cube is drawn from the S7 (for more details about the data release, see Thomas et al. 2017; Dopita et al. 2015). We extract the spectra of the marked pixels in the H α flux map (Fig. 12) and fit the profiles of the H α emission lines. We detect a similar effect as in the Br γ emission line.

We observe that the blue-shifted part of the line, in the spectra in Fig. 12 (bottom left) denoted with blue lines, is strongest in aperture II, which is in the north-west where the blue-shifted part of the large-scale rotational pattern is also located. The red-shifted part of the line, however, is stronger than the blue-shifted in aperture N; this is the only visible component in apertures I3

and I4, which are located in the south-east where the red-shifted part of the large-scale disc is located.

A jet or an outflow from the AGN, interacting with the galactic disc can result in a line split and radio emission. In NGC 1672 this seems not to be the case: we overlaid the contours of ATCA 3 cm radio data from Jenkins et al. (2011) on the Br γ flux map (Fig. 12). While the region with the prominent red-shifted second component of the Br γ gas emission coincides with the feature that connects the centre and the ring in the radio emission, Kakkad et al. (2018) ruled out the outflow scenario, since the [O III] emission line that they investigated in the S7 optical-blue spectra, has a width lower than 200 km s^{-1} .

The simplest explanation for the complex kinematics in NGC 1672 is that the velocity field of the Br γ emitting gas is not sampling the circumnuclear disc and rather is strongly weighted by the emission from the ILR ring. The doubled-horn line shape is then produced by the emission from the very strong knots in the ring. The latter is not axi-symmetric and can therefore cause an asymmetric velocity field. This is in contrast to the stellar velocity field which is weighted neither by the ring nor the nuclear disc and is therefore symmetric. As mentioned before, the Br γ velocity field is off-centred towards the north-west with the centre falling into aperture I2. Furthermore, the velocity gradient in the centre is strong, which can produce a double-horned line profile as well.

3.6. ILR star-forming ring

NGC 1672 has a well-known ILR ring (first imaged by Evans et al. 1996) located at the turnover point of the large-scale bar. Jenkins et al. (2011, their Fig. 8) presented the ring in several wavelengths (from 0.3–10 keV X-ray to 3 cm radio images). The ring has a semi-major axis of ~ 350 pc at a position angle of around 135° . It is clearly visible in our line maps, which are shown in Fig. 3 and trace the ionised regions (Br γ and He I), partially ionised regions ([Fe II]) and the hot molecular gas reservoir (H $_2$ (1–0)S(1)).

The emission line ratios $\log([\text{Fe II}]/\text{Br}\gamma)$ vs. $\log(\text{H}_2(1-0) \text{ S}(1) / \text{Br}\gamma)$ in the NIR diagnostic diagram (Fig. 6) indicate that excitation through young star formation dominates in the ring. Also the line ratios of molecular hydrogen emission lines (Fig. 7) indicate a significant contribution of non-thermal excitation, which is typical for young star formation (Sect. 3.3). Both of these indications confirm the star-forming nature of the ring.

Star formation rates. The luminosity of hydrogen recombination lines is proportional to the Lyman continuum and can therefore, in absence of an AGN, directly measure the instantaneous star formation rate. Using the luminosity of the Br γ

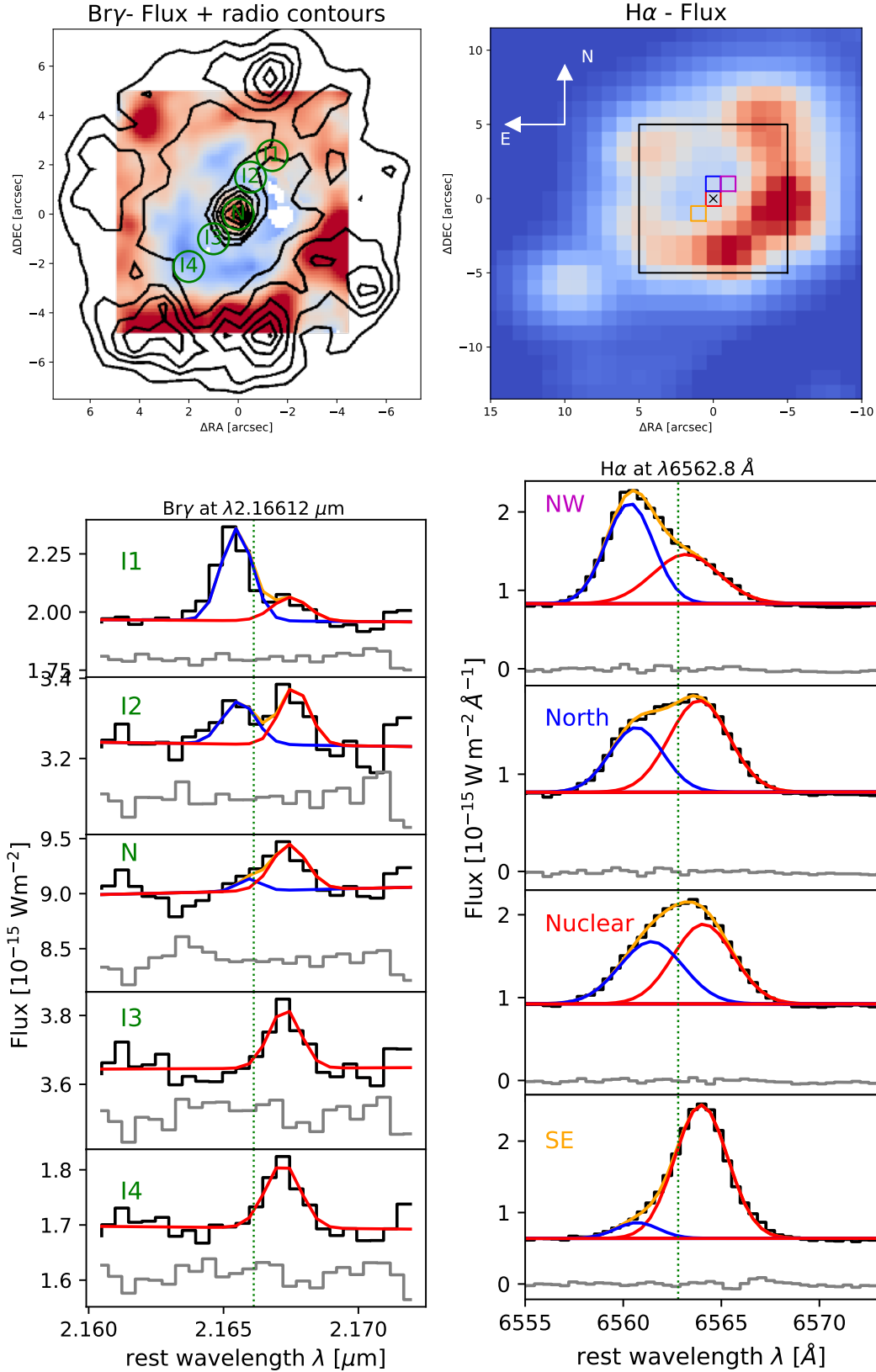


Fig. 12. *Top left:* flux map of the emission line $\text{Br}\gamma$ $2.16612 \mu\text{m}$. Overlaid are the radio contours from Jenkins et al. (2011), which have an angular resolution of $1''.3 \times 1''.0$. *Bottom left:* spectra near $\lambda = 2.16612 \mu\text{m}$ extracted from apertures I1-4 and N indicated in the flux map from north-west to south-east of the nucleus. For the I1-2 and N apertures at nucleus and to its north-west a line split is detected and a double-component Gaussian is used to fit the emission line. *Top right:* flux map of the emission line $\text{H}\alpha$ 6562.8 \AA . *Bottom right:* spectra of $\text{H}\alpha$ from the apertures indicated in the emission line flux map with spectral and angular resolutions of $R = 7000$ and $1''$ (Dopita et al. 2015), respectively; the spectra are extracted from $1'' \times 1''$ pixels. The green dotted lines show the rest wavelength of the emission lines. At the nucleus and NW a line split is detected and the emission lines need to be fitted with two-component Gaussian profiles (data from S7; Thomas et al. 2017).

emission line and the calibration from Panuzzo et al. (2003), we estimate the star formation rate (SFR) in the starburst regions:

$$\text{SFR} = \frac{L_{\text{Bry}}}{1.585 \times 10^{32} \text{W}} M_{\odot} \text{yr}^{-1}. \quad (5)$$

The SFR of the apertures are listed in Table 3 and the values are in the range $0.01\text{--}0.05 M_{\odot} \text{yr}^{-1}$. We also estimate an upper limit for the SFR in the nuclear region of $0.04 M_{\odot} \text{yr}^{-1}$, however, the possible AGN contribution to production of the emission line has to be considered.

Star formation scenarios. Star formation scenarios in ILR rings are still under discussion. Böker et al. (2008) suggested to distinguish between the so-called pearls-on-a-string and popcorn models. In the first, star formation is triggered at the touch-points of ring and spirals where gas is compressed and the star-forming regions then age while travelling along the ring. In the latter model, star formation occurs stochastically within the ring.

We compared the emission line maps of He I which has a high ionisation potential of 24.6 eV and can therefore only be ionised by the most massive O and B stars which have short lifetimes of $\lesssim 5$ Myr; Bry, which has a lower ionisation potential of 13.6 eV; and [Fe II], which can trace supernovae that become frequent after ~ 10 Myr when the most massive and short-lived stars explode in supernovae. In this comparison, we cannot see any gradient. Therefore, we conclude that there is no evidence for a sequence in star formation but the star formation is rather occurring stochastically along the ring.

3.7. Nature of the nuclear source

Classification of the nucleus in NGC 1672 has been complicated, partially because of the contamination of observations of the nucleus with the emission coming from strong star formation in the circumnuclear ring, which are mixed in observations with lower angular resolution. Therefore the nucleus was classified as a composite Seyfert 2/Starburst, where starburst dominates (e.g. Kewley et al. 2000; Storchi-Bergmann et al. 1995).

Similarly, in the X-ray wavelength, different classifications occurred owing to a lack of spatial resolution (Brandt et al. 1996; de Naray et al. 2000). However, Jenkins et al. (2011) using high-resolution *Chandra* data detected the nucleus in hard X-ray emission ($\Gamma \sim 1.5$, $L_{2\text{--}10\text{keV}} = 4 \times 10^{38} \text{erg s}^{-1}$) for the first time. Therefore they concluded that there is a low-luminosity active galactic nucleus (LLAGN) at the centre of NGC 1672.

The spatial resolution of SINFONI also gives us the opportunity to study this region isolated from the circumnuclear starburst ring. The only ionised emission lines we detect in this region are Bry and [Fe II]. However, as we show in Fig. 11, the spectra are very noisy and the emission lines have a low signal-to-noise ratio. For the spectra shown in this figure we did not subtract the stellar continuum. Several molecular hydrogen emission lines are observed at the nucleus and the amount of gas in the nuclear aperture ($25 M_{\odot}$) is up to five times the star-forming knots in the star-forming ring. A cold molecular gas mass of $2.5 \times 10^7 M_{\odot}$ is found in the central torus by Combes et al. (2019) using CO(3–2) emission. The emission line ratios in the diagnostic diagram Fig. 6 show a value at the border of AGN and starburst nature for the nucleus aperture of NGC 1672.

The ratio $\text{H}_2(1\text{--}0)\text{S}(1)/\text{Bry}$ in the nuclear aperture is 1. This value is usually $\lesssim 0.6$ in starburst galaxies, $0.6\text{--}6$ in Seyferts, and >6 in low ionisation nuclear emission regions (LINER; e.g. Mazzalay et al. 2013). The ratio measured for NGC 1672 is consistent with low-luminosity AGNs (Seyfert2). We

therefore conclude that our measurements support the classification of NGC 1672 as a weak AGN.

SMBH mass

We estimated the mass of the central supermassive black hole (SMBH) by fitting the stellar velocity dispersion in an aperture of $3''$ radius at the centre. The aperture size was chosen to avoid the nuclear star-forming ring. As discussed in Sect. 3.5.1, the star-forming ring shows a lower stellar velocity dispersion which resembles the cold molecular gas of the underlying gas reservoir rather than that of the central spheroidal component.

Similar to Sect. 3.5.1, we applied the PPXF method with the same settings and measured a velocity dispersion value of $\sigma = (106 \pm 3) \text{km s}^{-1}$. We now employ the $M\text{--}\sigma_*$ relation from Kormendy & Ho (2013)

$$\log\left(\frac{M_{\text{BH}}}{M_{\odot}}\right) = 8.5 + 4.41 \times \log\left(\frac{\sigma_*}{200 \text{km s}^{-1}}\right). \quad (6)$$

Using this relation and the fitted σ_* value, we derive a black hole mass estimate of $\log(M_{\text{BH}}/M_{\odot}) = 7.3$. Considering that the intrinsic scatter of the $M_{\text{BH}}\text{--}\sigma$ relation is higher than the measurements error, we refrain from stating formal errors on the BH mass estimates and the value reported in this work is an order of magnitude estimate.

This value is consistent with other black hole mass estimates in the literature: for example, Davis et al. (2014) derive $\log(M_{\text{BH}}/M_{\odot}) = (7.08 \pm 0.90)$ for NGC 1672 using the relation between black hole mass and spiral arm pitch angle. The Seric index of the central spheroidal component is $n = (2.05 \pm 0.17)$ according to Fisher & Drory (2010). Using the $M\text{--}n$ relation of Graham & Driver (2007) we then derive an estimate $\log(M_{\text{BH}}/M_{\odot}) = 7.3$, which is similar to our result. On the other hand, Combes et al. (2019) found a black hole mass of $\log(M_{\text{BH}}/M_{\odot}) = (7.7 \pm 0.1)$ as a best-fit estimate from the CO molecular gas dynamics, which is significantly higher.

An issue to keep in mind in this context is that the central component of NGC 1672 seems to be of pseudo-bulge nature (Fisher & Drory 2010). There have been lively discussions on the nature of pseudo-bulges and whether they show correlations with properties of the central SMBH (e.g. Kormendy et al. 2011; Graham 2016). In that sense, the higher estimate from the gas dynamics would be more adequate in this case. Given the uncertainties, we only conclude that the mass of central SMBH is of the order of several $10^7 M_{\odot}$, which is a typical mass for SMBHs in nearby galaxies (e.g. Greene & Ho 2005; Busch et al. 2017; Humire et al. 2018; Slater et al. 2019; Fazeli et al. 2019).

4. Summary and conclusions

In this paper we have presented a comprehensive analysis of the NIR IFS data for the central $10'' \times 10''$ ($550 \times 550 \text{pc}^2$) of the Seyfert galaxy NGC 1672. The data was obtained with the instrument SINFONI at the VLT. The following summarises our most important results:

- The most prominent feature detected in the emission line flux maps is the ILR star-forming ring. The ring is located at a radius of about $4'' \sim 220 \text{pc}$ from the centre and contains patchy starburst regions. The emission is asymmetric and stronger in the south and east.
- We find a hot molecular gas mass of $\sim 260 M_{\odot}$, using the $\text{H}_2 \lambda 2.122 \mu\text{m}$ emission line flux and assuming a local thermal equilibrium with temperature $T = 2000 \text{K}$. This amount corresponds to $(0.6\text{--}3) \times 10^8 M_{\odot}$ of cold molecular gas mass.

- We also estimate the ionised gas mass to $\sim 2.3 \times 10^6 M_{\odot}$, using the flux of the hydrogen recombination emission line Bry and assuming a temperature of $T = 10^4$ K and electron density of $n_e = 10^2 \text{ cm}^{-2}$. The ionised gas is mostly concentrated in the star-forming ring.
- The fits of stellar CO band head absorption lines are used to study the stellar kinematics. The LOSV map shows a rotating disc in the plane of the galaxy, which is blue-shifted in the north-west and red-shifted in the south-east of the FOV.
- Gas kinematics show a similar rotation pattern to the stellar disc, blue-shifted in the north-west and red-shifted in the south-east. However, the comparison of the stellar and gas kinematics reveals that the gas has much higher velocity amplitudes north-west and south-east of the nucleus, within the ILR ring, which can partially be attributed to a significant fraction of the kinematic energy of the stars going into random motions. Furthermore, the gas kinematics reveal non-circular motions.
- The position angle of the H₂ molecular gas and [Fe II] emission changes from the large scale to the central arcsec, resembling the decoupled nuclear disc or molecular torus found in CO(3–2). Furthermore, a double-horn Bry emission line profile is found at the nucleus and north-west of the centre, which spatially coincides with a filament in the 3 cm radio emission map, connecting the centre and the star-forming ring.
- The diagnostics diagram, using the H₂(1–0)S(1) $\lambda 2.122 \mu\text{m}$ /Bry and [Fe II] $\lambda 1.644 \mu\text{m}$ /Bry line ratios, suggests that the galaxy has a low-luminosity AGN. We estimated the black hole mass, based on black hole mass – host galaxy scaling relations, to be of the order of several $10^7 M_{\odot}$.

Acknowledgements. The authors thank the anonymous referee for fruitful comments and suggestions. This research is carried out within the Collaborative Research Center 956, sub-project A2 (the studies of the conditions for star formation in nearby AGN and QSOs), funded by the Deutsche Forschungsgemeinschaft (DFG) – project ID 184018867. N. Fazeli is a member of the Bonn-Cologne Graduate School of Physics and Astronomy (BCGS). M. Yttergren is a member of the International Max Planck Research School for Astronomy & Astrophysics Bonn/Cologne.

References

- Baumgart, C. W., & Peterson, C. J. 1986, *PASP*, **98**, 56
- Black, J. H., & van Dishoeck, E. F. 1987, *ApJ*, **322**, 412
- Blitz, L. 1994, in *Physics of the Gaseous and Stellar Disks of the Galaxy*, ed. I. R. King, *ASP Conf. Ser.*, **66**, 1
- Böker, T., Falcón-Barroso, J., Schinnerer, E., Knapen, J. H., & Ryder, S. 2008, *AJ*, **135**, 479
- Bonnet, H., Abuter, R., Baker, A., et al. 2004, *The Messenger*, **117**, 17
- Brand, P. W. J. L., Toner, M. P., Geballe, T. R., et al. 1989, *MNRAS*, **236**, 929
- Brandt, W. N., Halpern, J. P., & Iwasawa, K. 1996, *MNRAS*, **281**, 687
- Busch, G., Eckart, A., Valencia-S., M., et al. 2017, *A&A*, **598**, A55
- Calzetti, D., Armus, L., Bohlin, R. C., et al. 2000, *ApJ*, **533**, 682
- Cappellari, M. 2017, *MNRAS*, **466**, 798
- Cappellari, M., & Emsellem, E. 2004, *PASP*, **116**, 138
- Colina, L., Piqueras López, J., Arribas, S., et al. 2015, *A&A*, **578**, A48
- Combes, F., García-Burillo, S., Casasola, V., et al. 2013, *A&A*, **558**, A124
- Combes, F., García-Burillo, S., Casasola, V., et al. 2014, *A&A*, **565**, A97
- Combes, F., García-Burillo, S., Audibert, A., et al. 2019, *A&A*, **623**, A79
- Davis, B. L., Berrier, J. C., Johns, L., et al. 2014, *ApJ*, **789**, 124
- de Naray, P. J., Brandt, W. N., Halpern, J. P., & Iwasawa, K. 2000, *AJ*, **119**, 612
- de Vaucouleurs, G., de Vaucouleurs, A., Corwin, H. G., Jr., et al. 1991, *Third Reference Catalogue of Bright Galaxies*
- Díaz, R., Carranza, G., Dottori, H., & Goldes, G. 1999, *ApJ*, **512**, 623
- Dopita, M. A., Shastri, P., Davies, R., et al. 2015, *ApJS*, **217**, 12
- Draine, B. T., & Woods, D. T. 1990, *ApJ*, **363**, 464
- Eisenhauer, F., Abuter, R., Bickert, K., et al. 2003, in *Instrument Design and Performance for Optical/Infrared Ground-based Telescopes*, eds. M. Iye, & A. F. M. Moorwood, *SPIE Conf. Ser.*, **4841**, 1548
- Evans, I. N., Koratkar, A. P., Storchi-Bergmann, T., et al. 1996, *ApJS*, **105**, 93
- Fabricius, M. H., Saglia, R. P., Fisher, D. B., et al. 2012, *ApJ*, **754**, 67
- Fazeli, N., Busch, G., Valencia-S., M., et al. 2019, *A&A*, **622**, A128
- Fiore, F., Feruglio, C., Shankar, F., et al. 2017, *A&A*, **601**, A143
- Firpo, V., Díaz, R., Dottori, H., et al. 2017, *Bol. Asoc. Argent. Astron. Plata Argent.*, **59**, 127
- Fisher, D. B., & Drory, N. 2010, *ApJ*, **716**, 942
- García-Burillo, S., & Combes, F. 2012, *J. Phys. Conf. Ser.*, **372**, 012050
- García-Burillo, S., Combes, F., Schinnerer, E., Boone, F., & Hunt, L. K. 2005, *A&A*, **441**, 1011
- García-Rissmann, A., Vega, L. R., Asari, N. V., et al. 2005, *MNRAS*, **359**, 765
- Glass, I. S. 1984, *MNRAS*, **211**, 461
- Graham, A. W. 2016, in *Galactic Bulges*, eds. E. Laurikainen, R. Peletier, & D. Gadotti, *Astrophys. Space Sci. Lib.*, **418**, 263
- Graham, A. W., & Driver, S. P. 2007, *ApJ*, **655**, 77
- Greene, J. E., & Ho, L. C. 2005, *ApJ*, **627**, 721
- Grosbøl, P., & Dottori, H. 2012, *A&A*, **542**, A39
- Gültekin, K., Richstone, D. O., Gebhardt, K., et al. 2009, *ApJ*, **698**, 198
- Ho, L. C., Li, Z.-Y., Barth, A. J., Seigar, M. S., & Peng, C. Y. 2011, *ApJS*, **197**, 21
- Hollenbach, D., & McKee, C. F. 1989, *ApJ*, **342**, 306
- Hopkins, P. F., & Quataert, E. 2010, *MNRAS*, **407**, 1529
- Howell, S. B. 2000, *Handbook of CCD Astronomy* (Cambridge: Cambridge University Press)
- Humire, P. K., Nagar, N. M., Finlez, C., et al. 2018, *A&A*, **614**, A94
- Jenkins, L. P., Brandt, W. N., Colbert, E. J. M., et al. 2011, *ApJ*, **734**, 33
- Kakkad, D., Groves, B., Dopita, M., et al. 2018, *A&A*, **618**, A6
- Kewley, L. J., Heisler, C. A., Dopita, M. A., et al. 2000, *ApJ*, **530**, 704
- Kim, W.-T., & Elmegreen, B. G. 2017, *ApJ*, **841**, L4
- Kormendy, J., & Ho, L. C. 2013, *ARA&A*, **51**, 511
- Kormendy, J., Bender, R., & Cornell, M. E. 2011, *Nature*, **469**, 374
- Lançon, A., Hauschildt, P. H., Ladjal, D., & Mouhcine, M. 2007, *A&A*, **468**, 205
- Maiolino, R., Rieke, G. H., & Rieke, M. J. 1996, *AJ*, **111**, 537
- Makarov, D., Prugniel, P., Terekhova, N., Courtois, H., & Vauglin, I. 2014, *A&A*, **570**, A13
- Maloney, P. R., Hollenbach, D. J., & Tielens, A. G. G. M. 1996, *ApJ*, **466**, 561
- Markwardt, C. B. 2009, in *Astronomical Data Analysis Software and Systems XVIII*, eds. D. A. Bohlender, D. Durand, & P. Dowler, *ASP Conf. Ser.*, **411**, 251
- Martini, P., Pogge, R. W., Ravindranath, S., & An, J. H. 2001, *ApJ*, **562**, 139
- Mazzalay, X., Saglia, R. P., Erwin, P., et al. 2013, *MNRAS*, **428**, 2389
- Mazzalay, X., Maciejewski, W., Erwin, P., et al. 2014, *MNRAS*, **438**, 2036
- Moser, L., Zuther, J., Busch, G., Valencia-S., M., & Eckart, A. 2012, *Proceedings of Nuclei of Seyfert Galaxies and QSOs – Central Engine & Conditions of Star Formation (Seyfert 2012)*, 6–8 November, 69
- Mouri, H. 1994, *ApJ*, **427**, 777
- Newville, M., Stensitzki, T., Allen, D. B., & Ingargiola, A. 2014, <https://doi.org/10.5281/zenodo.11813>
- Osterbrock, D. E. 1989, *Astrophysics of Gaseous Nebulae and Active Galactic Nuclei* (Mill Valley: University Science Books)
- Panuzzo, P., Bressan, A., Granato, G. L., Silva, L., & Danese, L. 2003, *A&A*, **409**, 99
- Riffel, R., Riffel, R. A., Ferrari, F., & Storchi-Bergmann, T. 2011, *MNRAS*, **416**, 493
- Riffel, R. A., Storchi-Bergmann, T., & Winge, C. 2013a, *MNRAS*, **430**, 2249
- Riffel, R., Rodríguez-Ardila, A., Aleman, I., et al. 2013b, *MNRAS*, **430**, 2002
- Riffel, R. A., Colina, L., Storchi-Bergmann, T., et al. 2016, *MNRAS*, **461**, 4192
- Rodríguez-Ardila, A., Pastoriza, M. G., Viegas, S., Sigut, T. A. A., & Pradhan, A. K. 2004, *A&A*, **425**, 457
- Rodríguez-Ardila, A., Riffel, R., & Pastoriza, M. G. 2005, *MNRAS*, **364**, 1041
- Scoville, N. Z., Hall, D. N. B., Ridgway, S. T., & Kleinmann, S. G. 1982, *ApJ*, **253**, 136
- Skrutskie, M. F., Cutri, R. M., Stiening, R., et al. 2006, *AJ*, **131**, 1163
- Slater, R., Nagar, N. M., Schnorr-Müller, A., et al. 2019, *A&A*, **621**, A83
- Smajić, S., Fischer, S., Zuther, J., & Eckart, A. 2012, *A&A*, **544**, A105
- Smajić, S., Moser, L., Eckart, A., et al. 2014, *A&A*, **567**, A119
- Smajić, S., Moser, L., Eckart, A., et al. 2015, *A&A*, **583**, A104
- Springel, V., Di Matteo, T., & Hernquist, L. 2005, *ApJ*, **620**, L79
- Steer, I., Madore, B. F., Mazzarella, J. M., et al. 2017, *AJ*, **153**, 37
- Sternberg, A., & Dalgarno, A. 1989, *ApJ*, **338**, 197
- Storchi-Bergmann, T., Kinney, A. L., & Challis, P. 1995, *ApJS*, **98**, 103
- Teixeira, T. C., & Emerson, J. P. 1999, *A&A*, **351**, 303
- Thomas, A. D., Dopita, M. A., Shastri, P., et al. 2017, *ApJS*, **232**, 11
- Veilleux, S., Cecil, G., & Bland-Hawthorn, J. 2005, *ARA&A*, **43**, 769
- Winge, C., Riffel, R. A., & Storchi-Bergmann, T. 2009, *ApJS*, **185**, 186
- Wolniewicz, L., Simbotin, I., & Dalgarno, A. 1998, *ApJS*, **115**, 293